

Bee⁺: A 95-mg Four-Winged Insect-Scale Flying Robot Driven by Twinned Unimorph Actuators

Xiufeng Yang, Ying Chen, Longlong Chang, Ariel A. Calderón, and Néstor O. Pérez-Arancibia

Abstract— We introduce Bee⁺, a 95-mg four-winged microrobot with improved controllability and open-loop-response characteristics with respect to those exhibited by state-of-the-art two-winged microrobots with the same size and similar weight (i.e., the 75-mg Harvard RoboBee and similar prototypes). The key innovation that made possible the development of Bee⁺ is the introduction of an extremely light (28-mg) pair of twinned unimorph actuators, which enabled the design of a new microrobotic mechanism that flaps four wings independently. A first main advantage of the proposed design, compared to two-winged RoboBee-like flyers, is that by increasing the number of actuators from two to four, the number of direct control inputs increases from three (roll-torque, pitch-torque and thrust-force) to four (roll-torque, pitch-torque, yaw-torque and thrust-force) when simple sinusoidal excitations are employed. A second advantage of Bee⁺ is that its four-wing configuration and flapping mode naturally damped the rotational disturbances that commonly affect the yaw degree of freedom of two-winged microrobots. In addition, the design of Bee⁺ greatly reduces the complexity of the associated fabrication process compared to those of other microrobots, as the unimorph actuators are fairly easy to build. Lastly, we hypothesize that given the relatively low wing-loading affecting their flapping mechanisms, the life expectancy of Bee⁺ must be considerably higher than those of the two-winged counterparts. The functionality and basic capabilities of Bee⁺ are demonstrated through a set of simple control experiments. We anticipate that this new platform will enable the implementation of high-performance controllers for the execution of high-speed aerobatic maneuvers at the sub-100-mg scale as well as diversifying the lines of research in the quest for achieving full autonomy at the sub-gram scale.

I. INTRODUCTION

Insect-sized aerial robots have the potential to be employed in a great number of tasks such as infrastructure inspection, search and rescue after disasters, artificial pollination, reconnaissance, surveillance, et cetera, which has motivated the interest of many research groups. Consistently, as an emerging field, research on cm-scale flapping-wing robots driven by piezoelectric actuators has produced numerous design innovations over the course of more than two decades. However, to date, no robot has been demonstrated to be capable of replicating the astounding capabilities displayed by flying insects [1], [2]. An obstacle that has limited progress is the fact that unlike insects which simultaneously use multiple distributed muscles for flapping and control [3], flapping-wing flying robots are driven by a small number of discrete actuators due to stringent constraints in size and weight, as well as fabrication challenges. In specific, all the insect-scale flying microrobots developed thus far operate underactuated during flight, which greatly restricts their maneuverability. For example, the prototype in [4] is driven by a single

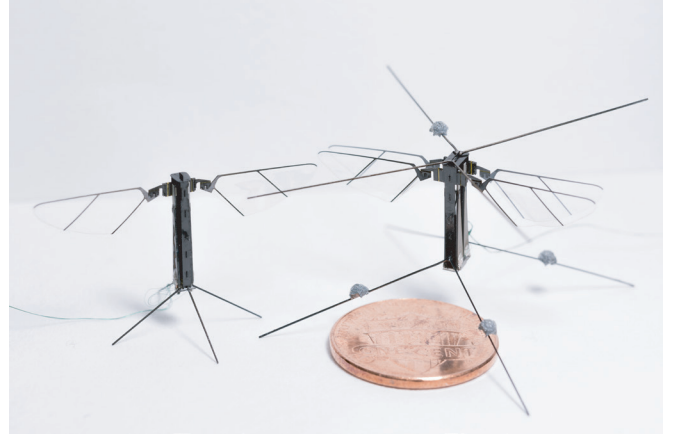


Fig. 1: We present the Bee⁺ (right), a new four-winged robot design. It has a mass of 95 mg and measures 33 mm in wing span. Four retroreflective markers (5 mg) for control are installed on its legs and protective spars. We also fabricated a two-winged robot (left) for comparison. It is adapted from the RoboBee [6] originally created at the *Harvard Microrobotics Laboratory*. A U.S. one-cent coin indicates the scale.

central piezoelectric bimorph actuator; therefore, it can only be controlled along the vertical direction while flying constrained by vertical guide wires [5].

In order to achieve controllability, based on the micro-fabrication technology in [4] and the ideas in [7], Harvard researchers developed the RoboBee, which is driven by two independent bimorph actuators [8]. Simple dynamic analyses indicate that this two-winged robot can directly generate control inputs to accelerate the its altitude, roll-angle and pitch-angle with sinusoidal flapping excitations, and the yaw *degree of freedom* (DOF) using *split-cycle* flapping [7]. Also, it can be shown that the horizontal translational variables can be controlled indirectly (also see [7]). Thus, in theory, RoboBee-like robots should be capable of readily performing basic flight maneuvers such as perching, landing, path following and obstacle avoidance [1] by controlling the six spatial degrees of freedom. However, during the performance real-time control experiments, it has been found that the yaw torque produced via *split-cycle* flapping is insufficient to overcome the restoring and damping forces opposing the yaw rotational motion of the robot [2].

Another solution to the controllability problem of the robot in [4], [5] is the three-actuator design presented in [11], which is composed of one central bimorph actuator employed for power and control, and two smaller lateral bimorph actuators used exclusively for control. Even though this robot can roll and pitch, its inability to steer has prevented it from performing agile flying maneuvers. Recently, following an approach that deviates from the bioinspiration paradigm, a 143-mg four-winged design was proposed in [2]. This robot (dubbed Four-wings) is composed of four bimorph actuators configured horizontally to form a 90-degree cross, thus resembling the

This work was supported by the *National Science Foundation* (NSF) through NRI Award 1528110 and the USC Viterbi School of Engineering.

The authors are with the Department of Aerospace and Mechanical Engineering, University of Southern California (USC), Los Angeles, CA 90089-1453, USA (e-mail: xiufeng@usc.edu; chen061@usc.edu; longlongc@usc.edu; aacalder@usc.edu; perezara@usc.edu).

TABLE I: Comparison of parameters for Bee⁺, RoboBee and Four-wings

Robot	Total mass (mg)	Actuators mass (mg)	Wing span (mm)	Flapping frequency (Hz)	Lift force (mN)	Wing area (mm ²)
Bee ⁺	95	56	33	100	1.4	200
RoboBee	75	50	35	120	1.3	104
Four-wings	143	100	56	160	4	218

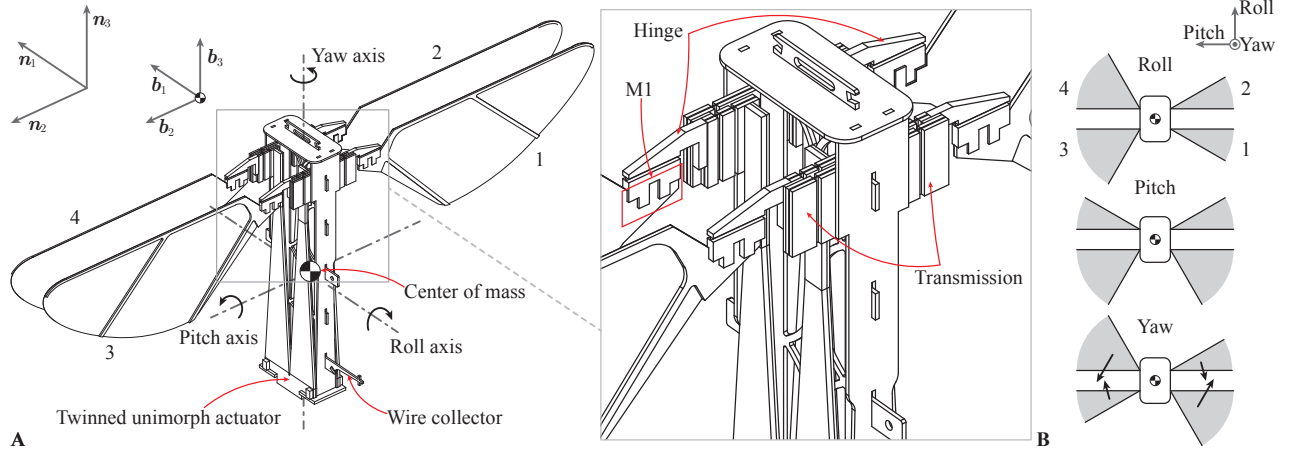


Fig. 2: Schematic diagrams for the four-winged robotic design: **A**. This figure shows the definition of the inertial frame, the body frame (shifted for clarity), the three body rotation axes, as well as the convention for numbers of wings and the configuration of the two twinned unimorph actuators. A detailed view of the wings, hinges, transmissions is shown in the middle. **B**. Torques generation strategy for all three orthogonal rotation axes for this four-winged design. Roll torque can be generated by varying the flapping amplitude difference between the left wings (3, 4) and the right wings (1, 2). Also, applying different flapping amplitudes on the front wings (2, 4) and the back wings (1, 3) would produce pitch torque. The steering motion along the yaw axis b_3 can be achieved with three different strategies [9], [10] on the four-winged robot as discussed in Section II-B. Here, we only demonstrate the strategy (iii): by adjusting the flapping amplitudes of the pairs of wings in diagonal direction, i.e. wings (1, 4) and wings (2, 3), projected components of the aerodynamic forces generated on the wings in b_1 - b_2 plane (indicated by the arrows) could produce corresponding yaw torques, meanwhile roll torques of the robot maintain approximately balanced. Flapping amplitudes are not to scale.

shape of a regular quadrotor. Due to its configuration, Four-wings exhibits a significantly-improved payload capacity compared to those of previous designs and can effectively steer, which suggests that it might be able to perform nontrivial controlled flying maneuvers. Note that these new capabilities directly follow from the fact that by increasing the number of actuators, the control authority is also increased (as the degree of underactuation decreases). This notion is clearly supported by research on larger-scale four-winged flying robots; for example, the DelFly Nimble [10] (with a weight of 29 g and a wingspan of 330 mm), which is equipped with two actuators for flapping, one actuator for dihedral-angle control and one actuator for wing-root control, is able to perform a large number of insect-inspired aerobatic maneuvers such as 360° flips and fast banked turns.

Here, motivated by the potential agility and controllability of flying robots with augmented actuation capabilities, we introduce Bee⁺, a new 95-mg insect-scale robotic design with four wings independently powered by two pairs of twinned unimorph actuators (Fig. 1). In this approach, rather than using four bimorph actuators as in [2], we employ four unimorph actuators twinned in two pairs as shown in Fig. 2 and fabricated monolithically as shown in Fig 3. In the final assembly of the robot, a pair of twinned actuators is installed on each side of the airframe to independently drive the four wings of the system through four individual micro-transmissions as depicted in Fig. 2-B. In this particular design, the wingspan of each wing is 33 mm and the maximum achievable thrust-force at 100 Hz is approximately 1.4 mN.

The main characteristics and parameters of Bee⁺, compared to those of the RoboBee and Four-wings are summarized in Table I. These data allows us to state the main characteristics of Bee⁺ in comparison to the best state-of-the-art insect-scale

robots thus far described in the technical literature:

- (i) A pair of twinned unimorph actuators weighs only 28 mg, i.e., only 3 mg more than a single bimorph actuator (25 mg) used in the fabrication of the RoboBee and Four-wings. Consequently, the total weight of Bee⁺ is not significantly higher than that of the two-winged RoboBee and is lighter than that of the Four-wings.
- (ii) Due to its compact configuration and the short wingspan of its wings (33 mm), the volume of the imaginary parallelepipedal envelop enclosing Bee⁺ is almost identical to that of the RoboBee and significantly smaller than that of Four-wings, which has its four actuators oriented horizontally.
- (iii) The total wing area of Bee⁺ is twice as large as that of the RoboBee while its weight is only 27 % higher, which significantly reduces the total *wing-loading* on the robot. Lower wing-loading not only reduces the forces and moments acting on the robot's actuators, which increases the life-expectancy of the mechanical components, but it is also advantageous from the aerodynamic design viewpoint. The details associated with this phenomenon are discussed in Section II-B.
- (iv) The novel design of the proposed twinned unimorph actuators, fabricated using the methods described in [12], significantly reduces the complexity of the fabrication process and the statistical frequency of assembling errors compared to that of the two-wing robots. Also, compared to Four-wings, the circuitry of the four actuators driving Bee⁺ is simpler as it requires only five output wires instead of six.

The rest of this paper is structured as follows. First, we describe the design of the proposed four-winged robot driven by twinned unimorph actuators (Bee⁺), as well as a basic aerodynamic analysis of the system. Then, we describe the fabrication process of the robot in detail, in which we mostly focus on the actuator manufacturing method. Next, we present

the process of controller synthesis and a set of controlled flight experiments. Finally, we draw some conclusions and discussed directions for future research.

II. DESIGN AND ANALYSIS

A. Robotic Design

It took years of innovation in microfabrication and actuator development for researchers to move the field of micro-robotics from the original single-actuator flying robot in [4] to the two-actuator RoboBee in [6]. Although multiple-actuator robotic configurations provide more options for the design and implementation of high-performance flight controllers, their development brings numerous challenges, especially in two main aspects. First, the integration of multiple actuators into a cm-scale airframe presents many difficulties from the fabrication perspective as the functionality and performance of microrobots greatly depend on the uniformity of the moving parts, symmetry of the structural components and precision of the final assembly. Second, in general, actuators are major contributors to the total weight of insect-sized robots (for example, $\geq 66\%$ in [4]); therefore, the addition of actuators to a robotic design requires the generation of significant more lift-force. In this work, we overcome this challenges by introducing an optimized way to integrate four actuators into the robot, thus taking one step further from the RoboBee.

A comparison of Bee⁺ with a two-winged robot is shown in Fig. 1. The most distinctive characteristic of Bee⁺ is its four-winged design compactly packaged inside a volume similar to that of the two-winged RoboBee. The detailed mechanical design is shown in Fig. 2-A, in which legs and protective spars are not shown for clarity. The robot has a symmetric configuration with respect to the b_1 - b_3 plane that separates the right and left sides of the body frame of reference; in this case, by convention, wings 1 and 2 are located in the right half-space and wings 3 and 4 are located in the left half-plane. Each wing flaps only within its corresponding quadrant defined by the body b_1 - b_2 plane, so less amplitude of deflection is required from each actuator compared to those in two-winged robot case. The key component that makes this design feasible is the pair of twinned unimorph actuators with a common base shown in Fig. 2-A. The fabrication method of these *single-body-multiple-output* (SBMO) actuation devices is described in Section III-A. Note that each pair of twinned unimorph actuators can be thought of as an unfolded bimorph actuator, which explain why the weight difference between these two types of actuation microdevices is of 3 mg only (the analog bimorph actuator is 3 mg lighter). In total, Bee⁺ is 20 mg heavier than the RoboBee due to other additional structural weight; this is not an issue, however, as Bee⁺ is able to generate sufficient thrust forces and aerodynamic moments for flying and control.

Because the two pair of twinned unimorph actuators are fabricated from the same composite stack and employing exactly the same process, their mechanical properties, functionalities and achieved performances are very similar. This fabrication methodology is simpler and more precise than pairing actuators (as done in [6]). Also, the use of twinned actuators eliminates the possibility of misalignment due to assembly errors on each side of the robot's body as each pair of unimorph actuators is a monolithic piece; thus, we only need to enforce the symmetry of the left side with respect to the right side. To power Bee⁺, a minimum of five wires is required: two for the driving signals of each pair of twinned unimorph actuators and one for the common ground. The details of the driving method are

discussed in Section III-A. To avoid tangling or disconnection when the robot is flying, the five wires are bundled and wrapped around the wire collector shown in Fig. 2-A.

B. Aerodynamic Design and Analysis

The proposed four-winged Bee⁺ (see Fig. 1 and Fig. 2-A), theoretically, has superior controllability capabilities compared to those exhibit by two-winged robots. However, there are two adverse factors that must be consider considered and studied: the increased total weight of the robot; and the fact that each wing is constrained to flap with amplitudes equal or smaller than 90° due to the geometry of the robotic design (see Fig. 2-A), which decreases the maximum thrust-force that each wing can generate. Therefore, when designing the robot, it is not a trivial issue to guarantee that the four wings are capable of generating sufficient thrust forces and aerodynamic moments to enable the robot to take off, stabilize itself and maneuver.

For a single wing with a sinusoidal flapping profile, the aerodynamic force due to the local velocity of the airflow and wing's angle of attack (i.e., the translational force in [13]) is the main contribution to the cycle-averaged lift

$$\bar{f}_L = C_L(\bar{\alpha}) \frac{1}{2} \rho (2\phi_0 \nu r_{\text{ref}})^2 S = C_L(\bar{\alpha}) \nu^2 \phi_0^2 S, \quad (1)$$

in which C_L is the cycle-averaged lift coefficient as a function of the aerodynamic mean angle of attack $\bar{\alpha}$; ρ is the density of the air; ϕ_0 is the end-to-end amplitude of the flapping angle; ν is the flapping frequency; r_{ref} is the location for the reference velocity; and S is the wing area. C_L is a combined coefficient that simplifies the expression.

Even though (1) is widely employed in the analysis of flapping-wing microrobots, this formula only provides a quick estimation of the cycle-averaged lift. Furthermore, for wings flapped through passive pitching mechanisms, the instantaneous values of the associated angles of attack are very difficult to predict as they are influenced by unsteady aerodynamic forces [13]; therefore, we lack a direct method to accurately estimate $\bar{\alpha}$. Here, we employ the numerical fluid-structure interaction method in [14] and the instantaneous aerodynamic models in [13] to estimate the aerodynamic forces produced by the wings. For purposes of aerodynamic design, ν is selected to be 100 Hz, the designed ϕ_0 is 65° , the limit for the wing pitching angles is 70° and the hinge stiffness, k_h , is designed to be $1.4 \mu\text{Nm}$. For these parameters and the wing geometry shown in Fig. 2-A, the calculated cycle-averaged lift is approximately 1.4 mN and the corresponding lift-to-weight ratio is approximately 1.4; hence, based on this analysis, Bee⁺ is capable of generating sufficient lift force for taking off, stabilizing itself and maneuvering. This result agrees with estimations performed using data from control experiments (see Section IV).

As discussed in [2], two-winged robots are not very effective at passively resisting rotational disturbances and/or actively steering the their bodies about the yaw axis b_3 . For the ease of analysis, the body b_1 - b_2 plane is defined as the *steering plane*. By noticing that for insect-scale microrobots the flapping frequency ν is significantly higher than the frequencies of the body oscillations [2], [13], the cycle-averaged damping force, \bar{f}_d , can be employed in the analysis of the yaw dynamics of the robot. Thus, for the upstroke and downstroke of a sinusoidal flapping pattern with symmetric profile, the cycle-averaged damping force [13], [15] is estimated as

$$\bar{f}_d = C_2(\bar{\alpha}) \phi_0 \nu \omega_b S + C_3(\bar{\alpha}) \dot{\omega}_b S, \quad (2)$$

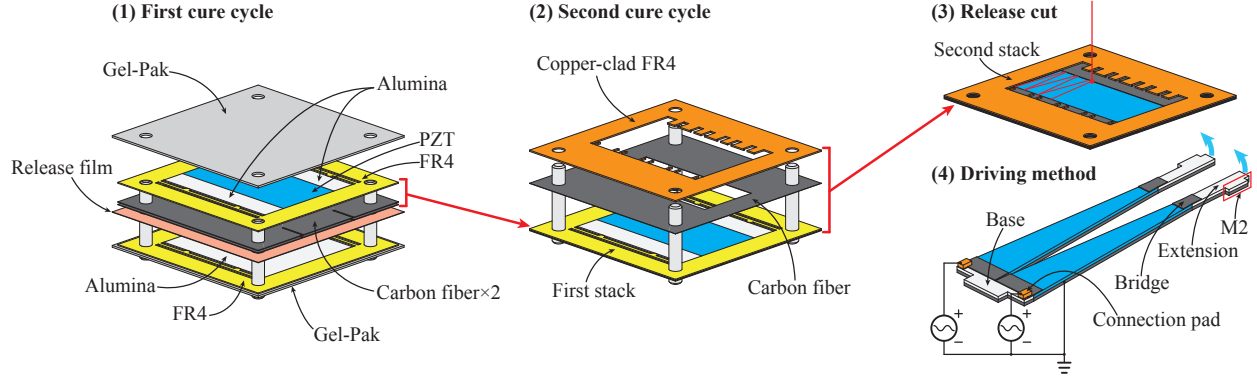


Fig. 3: Fabrication process of piezoelectric twinned unimorph actuators and driving method. (1): First cure cycle for the unimorph stack. The PZT ($127\mu\text{m}$) and alumina ($127\mu\text{m}$) laminates are bonded with two layers of high modulus carbon fiber composite ($63\mu\text{m}$ each) through applying heat (180°C) and pressure (15 psi) on the pin-aligned stack. The bottom layer of alumina works as a substrate for keeping the stack flat, and is prevented from being bonded by a layer of release film. (2): Second cure cycle for the stack. The unimorph stack yielded from the first step is cured with a layer of carbon fiber composite ($27\mu\text{m}$) and a layer of copper-clad FR4 ($137\mu\text{m}$) using the same curing method. (3) Laser release cut. Four sets of twinned actuators are release from the unimorph stack with laser cut from the top side. (4) Driving method. We can drive the twinned unimorph actuator using the circuitry as illustrated above. Two sinusoidal voltage signals with maximum magnitudes of 260 V are applied to power the actuator in this work, accordingly the two unimorphs bend upwards as indicated by the arrows. The length of a resulting twinned actuator is 13 mm .

where C_2 and C_3 are the combined coefficients derived from the instantaneous models in [13]. In (1), \bar{f}_L is proportional to $\phi_0^2 \nu^2 S$. Thus, given similar weights and a constant ω_b , from (2) it follows that Bee^+ can generate at least 1.4 times the damping force produced by a two-winged robot with a similar size. Note that if external disturbances cause large values of ω_b , the resulting damping force can even double the values of those corresponding to two-winged robots.

To enable yaw steering capabilities, the wings must be able to actively generate a non-zero net force f_s in the steering plane in one flapping cycle. From the conceptual design perspective, there are three feasible strategies available to generate a non-zero f_s : (i) *Split-cycle* [2], [16]. From simple analyses and experimental data obtained using the Four-wings prototype [2], it follows that this strategy requires a high actuation bandwidth for both frequency modulation and yaw-torque amplification, which is costly and difficult to achieve from the design and fabrication perspective. (ii) *Asymmetric angle of attack*. This is the method employed by the DelFly Nimble in [10], which uses an actuator to actively control the wing root; in this way, the angles of attack of the wing during the up- and down-strokes can be set to different values. (iii) *Inclined stroke plane*. This method consists in pre-setting or adjusting the stroke plane to have an angle (labeled with β) with respect to the steering plane. When the stroke plane is inclined, the aerodynamic force produced by a wing projects a non-zero component onto the steering plane.

For the two-winged configuration, the stroke plane angle must be actively controlled in order to achieve yaw steering, as exemplified in [9] employing a bird-sized flying robot. Note that active control of the stroke plane requires the use of complex actuation mechanisms. On the other hand, the four-winged configuration of Bee^+ can produce controllable yaw torques with a fixed stroke plane by employing the flapping scheme in Fig. 2-B. According to this scheme, one diagonal pair of wings (1 and 4) can produce yaw torques in the counter-clockwise direction while the other diagonal pair of wings (2 and 3) can generate clockwise yaw torques. Thus, by adjusting the flapping amplitudes of two pairs of wings, the robot can actively modulate the production of yaw torque. Furthermore, unlike in the two-winged case, by diagonally pairing the four wings, the modulation of the yaw-torque does not introduce significant undesirable roll torques as they

stay approximately balanced. From this simple analysis, we conclude that strategy (iii) requires minimum design and has a small fabrication cost; therefore, it is very advantageous for the design of insect-scale flying robots.

In addition, because torques about the three rotation axes can be controlled by adjusting the flapping amplitudes of four wings (see Fig. 2-B), the robot can be controlled during flight employing methods already developed for quadrotors. Consequently, we choose strategy (iii) for the conceptual design of Bee^+ . Detailed analytical and experimental results on yaw control will be presented in a future publication; here, we briefly discuss some ideas on a generalized yaw control strategy. Namely, the active yaw-torque generated by the projection of the cycle-averaged lift onto the steering plane can be calculated as

$$f_s = \bar{f}_L \sin \beta = C_4(\bar{\alpha}) \nu^2 \phi_0^2, \quad (3)$$

$$\tau_s = r_s f_s = C_5(\bar{\alpha}) \nu^2 \phi_0^2, \quad (4)$$

where r_s is the distance from the pressure center of the wing to the b_3 axis, and C_4 and C_5 are combined coefficients derived from the instantaneous models in [13]. Note that since in practice $\bar{\alpha}$ can vary along with ϕ_0 in a highly nonlinear manner, the models in (1), (3) and (4) cannot be used directly. With proper identification, however, these models can be approximated by using constant-coefficient linear models, as done in Section IV-D for flight controller synthesis.

Finally, it is important to state that compared to the case of two-winged robots, the wing-loading on Bee^+ is reduced by 34%. Lower wing-loading not only reduces the demands on the actuators, but also induces smaller deformations of the wings. This latter fact is relevant because large undesired wing deformations may cause unexpected force generations when the flapping amplitude is varied due to the actions of the flight control system. In addition, the maximum flapping amplitude can be greatly limited by non-negligible wing loading. In the two-winged configuration case, the typical operating flapping amplitudes oscillate around 110° . However, the designed value of ϕ_0 for Bee^+ not necessary has to be 55° as large amplitude ranges are desirable for both power and control. In static experiments (see supplementary movie S1.mp4), the maximum observed amplitudes achieve values of approximately 75° .

III. FABRICATION

A. Twinned Unimorph Actuator

The twinned unimorph actuator is the most critical component of the robotic mechanism (Fig. 2-A). It would be almost impossible to fabricate such SBMO actuator using the method of making bimorph actuators of RoboBee mentioned in [6]. Therefore, to build the actuators, we exploit one of the most recent custom actuator technology, the *pre-stack* method [12]. This method not only significantly improves the quality and consistency of the actuators, but also allows almost arbitrary planar design. In this work, we explored a new potential way of using this method: building the SBMO actuator. As an example for robotic application, we build the twinned unimorph actuators whose fabrication processes are illustrated in Fig. 3. Note that this process can be easily extended to monolithically manufacture multiple actuators with various shapes, dimensions or even orientations on one body.

The fabrication process includes two cure cycles and one laser release cut (Fig. 3). We use piezoelectric ceramics PZT-5H (T105-H4NO-2929, Piezo.com) as the *active layer* for the unimorph because of its high modulus and piezoelectric coefficient, and two layers of high modulus carbon fiber composite as the *passive layer* for achieving the equivalent stiffness of bimorph actuator [17]. The extension tip and base are made of alumina ceramics.

Before the first cure cycle, we cut all the laminate materials for the stacks using a precision diode-pumped solid-state (DPSS) laser (Photonics Industries DC150-355). The PZT, Alumina are initially cut into rectangles, cleaned with isopropyl alcohol in a sonicator to improve the adhesion during curing. The FR4 sheets are machined as jigs to hold these PZT and alumina pieces in position, forming two layers of the pin-aligned stack as shown in Fig. 3-(1). The lower one is placed on a Gel-Pak, a lightly tacky film sticking the alumina in place. Similarly, the upper layer is covered with a Gel-Pak. Through applying heat (180 °C) and pressure (15 psi) for two hours, the epoxy resin in the two central carbon fiber composite layers will cure and serve as adhesive to bond the upper layer together with the carbon fiber, forming the first stack as shown in Fig. 3-(2). The lower layer only serves as a rigid substrate to keep the first stack flat, and will not be bonded to the carbon fiber as a layer of release film isolates them from each other. For the second cure cycle, we apply the same temperature and pressure to laminate the first stack with an additional layer of carbon fiber composite and a copper-clad FR4 sheet. This carbon fiber will add “bridges” at the interfaces between the PZT and the Alumina, increasing the rigidity of the actuator. And the copper-clad FR4 will become the connection pads.

At last, the actuators with designed planar profiles are released from the second stack using laser cut. As our unimorph stack only has one layer of PZT at the top and one layer of cured carbon fiber composite at the bottom, we just need to cut once through all layers from the top as shown in Fig. 3-(3). This reduces the releasing time by half compared to that for releasing bimorphs, which requires one to cut twice, from the top and bottom side of the bimorph stack separately. The procedure of cutting-once-from-one-side also improves the yield of the actuators, since flipping the stack and realigning the laser cutting between the two cuttings for bimorph stack could introduce additional manufacturing errors causing cracks in PZT ceramics.

From one stack, the release cut yields total four pairs of twinned actuators. One of them is shown in Fig. 3-(4). It has

two identical unimorphs side by side, sharing one base. At the base, there is a clearance of 50 μm between the bottom edges of PZT splitting apart the two active PZT layers of two unimorphs. Their passive carbon fiber layers at the bottom side are connected, creating an inherent common ground. Therefore, to drive this actuator, we can employ the simple driver circuitry presented in Fig. 3-(4). Two independent voltage signals will be used to drive two unimorphs whose bending directions are indicated by the arrows when excited. In addition, conductive epoxy needs to be applied to electrically connect the copper pads and PZT layers before testing.

B. Assembly

The airframe, wings, hinges, transmissions, protective spars and legs are fabricated using *smart composite microstructures* process [18]. While detailed fabrication processes will not be discussed here, the specific assembling process should be explained because it is crucial for achieving the desired assembly relationships among all components. To begin with, three types of sub-assemblies are assembled separately. First one is airframe, including three pieces of carbon fiber and five pieces of FR4. Assembly relationships of these pieces are uniquely defined by their tab-and-slot features, where cyanoacrylate (CA) glue is also applied to create firm adhesion. Second one includes four wing-hinge sub-assemblies. Wings are attached to hinges with the toothed mating features (M1, highlighted in the detailed view of Fig. 2-A) using CA glue respectively. Third one includes two actuator-transmission sub-assemblies. Four transmissions are installed on the raised mating features of extension tips (M2, highlighted in Fig. 3-(4)) of two pairs of twinned unimorph actuators as the orientations shown in Fig. 2-A. Next, the actuator-transmission sub-assemblies are firmly glued onto the base of the airframe. We use orthogonal contact surfaces among the actuators and the base as constraints to guarantee the precision of assembling. Also, *ground linkages* of the transmissions are affixed to the airframe using glue. The last step is attaching the wing-hinge sub-assemblies to the transmissions. Their assembly relationships are less constrained, allowing final adjustments for compensating errors caused by previous steps.

IV. FLIGHT CONTROLLER DESIGN

A. System Dynamics

To describe the dynamics of Bee⁺, we define its body-fixed frame $\mathbf{b}_1\text{-}\mathbf{b}_2\text{-}\mathbf{b}_3$ as demonstrated in Fig. 2. Because the direction of thrust force is assumed to be aligned with the \mathbf{b}_3 axis and the number of actuators is less than the total number of the degree-of-freedom of the system, Bee⁺ is essentially a thrust-propelled underactuated system. Thus it can be viewed as a single rigid body with the dynamics described by:

$$m\ddot{\mathbf{r}} = -m\mathbf{g}\mathbf{n}_3 + \mathbf{f}\mathbf{b}_3, \quad (5)$$

$$\mathbf{J}\dot{\boldsymbol{\omega}} = -\boldsymbol{\omega} \times \mathbf{J}\boldsymbol{\omega} + \boldsymbol{\tau}, \quad (6)$$

$$\dot{\mathbf{q}} = \frac{1}{2}\mathbf{q} * \mathbf{p}, \quad (7)$$

where m is the total mass of the robot, $\mathbf{r} = [r_1 \ r_2 \ r_3]^T$ indicates the displacement of the center of mass relative to the origin of the inertial frame, and \mathbf{f} is the total thrust force generated by the flappings of the four wings. \mathbf{J} denotes the moment of the inertial of the robot, $\boldsymbol{\omega}$ is the flyer's angular velocity expressed in body frame with respect to the inertial frame, and $\boldsymbol{\tau}$ is the torque generated by the flappings of the wings. Quaternion \mathbf{q} is employed to describe the attitude of the robot relative to the inertial frame, quaternoin $\mathbf{p} = [0 \ \boldsymbol{\omega}^T]^T$,

and the symbol $*$ represents quaternion multiplication. In (5)(6) and (7), several assumptions are made; for example, the direction of the thrust forces is aligned with \mathbf{b}_3 ; the projection of the aerodynamic force generated by four wings' flappings onto the steering plane is assumed to be zero in one flapping circle, which yields that $f\mathbf{b}_3$ is the only external actuation force; the aerodynamic disturbances are ignored in (5)(6); the gyroscope effect between the wing flapping and body rotation is ignored as well. Overall, the dynamics of the Bee⁺ robot could employ the same single rigid body assumption as that of the quadrotor in [19].

B. Attitude Control

The desired attitude dynamics is given by

$$\dot{\mathbf{q}}_d = \frac{1}{2} \mathbf{q}_d * \mathbf{p}_d, \quad (8)$$

where \mathbf{q}_d is the quaternion representing the desired attitude and $\mathbf{p}_d = [0 \ \dot{\omega}_d^T]^T$, in which $\dot{\omega}_d$ denotes the desired angular velocity expressed in the desired frame \mathbf{q}_d . It follows that the attitude error between \mathbf{q} and \mathbf{q}_d can be described by the quaternion $\mathbf{q}_e = [m_e \ \mathbf{n}_e^T]^T$ given by

$$\mathbf{q}_e = \mathbf{q}_d^{-1} * \mathbf{q}. \quad (9)$$

And the attitude control torque is specified by

$$\boldsymbol{\tau} = -\mathbf{K}_1 \text{sgn}(m_e) \mathbf{n}_e - \mathbf{K}_2 (\boldsymbol{\omega} - \boldsymbol{\omega}_d), \quad (10)$$

where \mathbf{K}_1 and \mathbf{K}_2 are positive definite diagonal gain matrices, $\text{sgn}(\cdot)$ represents the sign function, and $\boldsymbol{\omega}_d$ denotes the desired angular velocity that has the exactly same components as $\dot{\omega}_d$ and is expressed in the body frame instead of the desired frame \mathbf{q}_d .

Denote the axis of the rotation from \mathbf{q} to \mathbf{q}_d by a unit vector \mathbf{a}_e , and the associated rotation angle is defined to be Θ_e , with $0 \leq \Theta_e < \pi$. Then, the term $-\text{sgn}(m_e) \mathbf{n}_e$ is geometrically equal to $\sin(\frac{1}{2}\Theta_e) \mathbf{a}_e$, and the multiplication of $\text{sgn}(m_e)$ is employed to remove the ambiguity of the quaternion representation since \mathbf{q}_e and $-\mathbf{q}_e$ represent the same rotation result.

C. Position Control

As the dynamics of Bee⁺ is an underactuated system with the direction of thrust force aligned with \mathbf{b}_3 axis, the position control of this system involves the specifications of the magnitude and the orientation of the thrust force, similar to other flapping-wing robots and the quadrotors [8] [20]. Therefore, the position control design is comprised of the generations of the desired thrust force magnitude and the desired attitude.

The magnitude of the thrust force is designed to be

$$f = f_a^T \mathbf{b}_3, \quad (11)$$

$$\begin{aligned} \mathbf{f}_a = & -\mathbf{K}_p (\mathbf{r} - \mathbf{r}_d) - \mathbf{K}_d (\dot{\mathbf{r}} - \dot{\mathbf{r}}_d) \\ & - \mathbf{K}_i \int (\mathbf{r} - \mathbf{r}_d) dt + m \mathbf{g} \mathbf{n}_3 + m \ddot{\mathbf{r}}_d, \end{aligned} \quad (12)$$

where \mathbf{K}_p , \mathbf{K}_d , \mathbf{K}_i are positive definite diagonal gain matrices, and \mathbf{r}_d is the desired position of the center of mass.

Next, the desired attitude is derived from the desired thrust force \mathbf{f}_a and the desired yaw angle ψ_d as follows:

$$\mathbf{b}_{3d} = \frac{\mathbf{f}_a}{\|\mathbf{f}_a\|_2}, \quad (13)$$

$$\mathbf{b}_{1d} = \frac{[-\sin \psi_d \ \cos \psi_d \ 0]^T \times \mathbf{b}_{3d}}{\|[-\sin \psi_d \ \cos \psi_d \ 0]^T \times \mathbf{b}_{3d}\|_2}, \quad (14)$$

$$\mathbf{b}_{2d} = \mathbf{b}_{3d} \times \mathbf{b}_{1d}, \quad (15)$$

where \mathbf{b}_{1d} , \mathbf{b}_{2d} , \mathbf{b}_{3d} are the desired axes of the body frame expressed in the inertial frame. Then, rotation matrix $\mathbf{S}_d = [\mathbf{b}_{1d} \ \mathbf{b}_{2d} \ \mathbf{b}_{3d}]$ describes the desired attitude, from which the desired attitude quaternion \mathbf{q}_d can be derived.

D. Actuator Command Generation

As discussed in Section II-B, each actuator is driven by a sinusoidal signal at 100 Hz with adjustable magnitude. Simplified from the models in (1)(3)(4), the thrust force of each flapping wing is approximately modeled as $f_i = k_f v_i$, with $i = 1, 2, 3, 4$, where f_i is the thrust force generated by the flapping of the i -th wing, v_i is the magnitude of the sinusoidal command signal of the i -th unimorph actuator, and k_f is the coefficient between the thrust force and the command magnitude. As illustrated in Fig. 2-B, yaw torques in the steering plane can be generated by employing the strategy (iii) mentioned in Section II-B. This projected component of the aerodynamic force on the steering plane is modeled as $f_{si} = k_s v_i$, with $i = 1, 2, 3, 4$, where f_{si} is the projected component of the aerodynamic force of the i -th wing and k_s is the coefficient between the force and the command magnitude. Thereby, the mapping between the thrust force and control torques and the actuator commands is given by

$$\begin{bmatrix} f \\ \tau_1 \\ \tau_2 \\ \tau_3 \end{bmatrix} = \begin{bmatrix} k_f & k_f & k_f & k_f \\ -k_f d_1 & -k_f d_1 & k_f d_1 & k_f d_1 \\ k_f d_2 & -k_f d_2 & k_f d_2 & -k_f d_2 \\ k_s d_3 & -k_s d_3 & -k_s d_3 & k_s d_3 \end{bmatrix} \begin{bmatrix} v_1 \\ v_2 \\ v_3 \\ v_4 \end{bmatrix}, \quad (16)$$

where d_i refers to the lever arm of the corresponding torque τ_i . It is straightforward that the mapping in (16) is similar to the mapping between the rotors' speeds and the control force and torques of the quadrotor [21]. Additionally, the four-winged design brings more control capability than the two-winged design [8] since the thrust force and the control torques are shared by four wings rather than two. Taking the inverse of (16) yields the mapping from the thrust force and torques to the actuator commands as

$$\begin{bmatrix} v_1 \\ v_2 \\ v_3 \\ v_4 \end{bmatrix} = \begin{bmatrix} \frac{1}{4k_f} & -\frac{1}{4d_1 k_f} & \frac{1}{4d_2 k_f} & \frac{1}{4d_3 k_h} \\ \frac{1}{4k_f} & -\frac{1}{4d_1 k_f} & -\frac{1}{4d_2 k_f} & -\frac{1}{4d_3 k_h} \\ \frac{1}{4k_f} & \frac{1}{4d_1 k_f} & \frac{1}{4d_2 k_f} & -\frac{1}{4d_3 k_h} \\ \frac{1}{4k_f} & \frac{1}{4d_1 k_f} & -\frac{1}{4d_2 k_f} & \frac{1}{4d_3 k_h} \end{bmatrix} \begin{bmatrix} f \\ \tau_1 \\ \tau_2 \\ \tau_3 \end{bmatrix}. \quad (17)$$

V. EXPERIMENTAL RESULTS

A. Experimental Setup

The experiment architecture includes the four-winged flying robot Bee⁺, four piezo-actuator drivers (PiezoMaster VP7206), Vicon Motion Capture system and the ground computer for processing data and generating real-time control signals. The Matlab Simulink Real-Time is used for processing the sensor measurements and generating the control signal with the control algorithm embedded in the ground computer. The control algorithm runs at a frequency of 2 kHz and the Vicon motion capture system measures the position and attitude states at a frequency of 500 Hz. The angular velocity cannot be directly measured via the motion capture system, thereby is estimated as the following:

$$\begin{bmatrix} 0 \\ \boldsymbol{\omega} \end{bmatrix} = 2\mathbf{q}^{-1} * \left[\frac{\lambda s}{s + \lambda} \right] \mathbf{q}, \quad (18)$$

where λ is the filter parameter, s is the complex variable of the Laplace transform, the bracket $[\cdot]$ represents the filter that operates on the signal \mathbf{q} . A similar low pass derivative filter operates on the position states to estimate the translational velocities. Note that the low pass filter is necessary for this aerial robotic system with high flapping frequency since the inertial force induced by the wing flapping introduces the unavoidable high magnitude oscillation of the robot body.

The open-loop trimming flight tests required in [8] [22] are not needed in the controlled flight of the four-winged

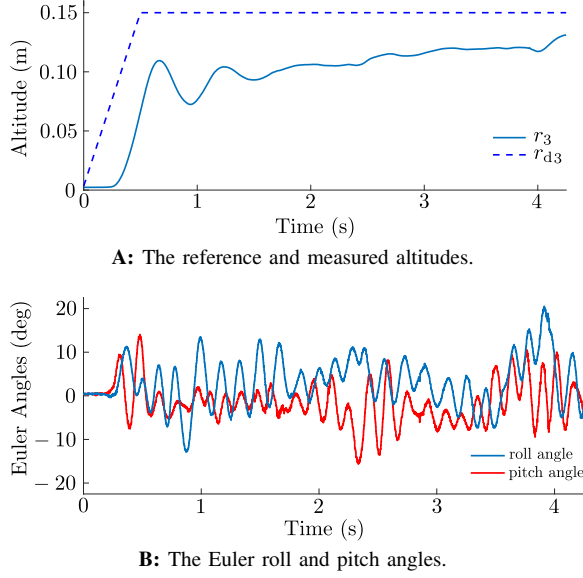


Fig. 4: The altitude and attitude control experimental results. **A.** It demonstrates the altitude in the experiment, in which the dash line represents the reference altitude. **B.** It shows the Euler roll and pitch angles during the experiment. Note that the angular oscillation remain approximately between -10° and 10° , which is partially caused by the oscillation of the robot body induced by the wing flapping and stays in an acceptable range. The experiment lasts for approximately 5 s, and after that the robot flies out of the specified safety space and the power is then turned off automatically.

flying robot proposed in this paper, implying that the control algorithm introduced in this work does not need the tuning of the command signals for the zero offset torques. This advantage significantly improves the efficiency of experiments.

B. Altitude and Attitude Control Experiment

The objective of the altitude and attitude control experiment is to control the robot to fly at a desired altitude with the direction of the thrust force remaining perpendicular to the \mathbf{n}_1 - \mathbf{n}_2 plane. In this preliminary control experiment, yaw feedback control is not applied to reduce the control burden of the four flapping wings, however the increased aerodynamic damping forces improve the open-loop stability of the yaw motion as discussed in Section. II-B. Additionally, the direction of the thrust force (i.e. \mathbf{b}_3) is theoretically irrelevant with the Euler yaw angle. Therefore, the control objective in the altitude and attitude control experiment is to regulate the altitude to a desired value, and to regulate the Euler roll and pitch angles to zero. It follows that the desired attitude quaternion in the altitude and attitude control experiment is given by

$$\mathbf{q}_d = \begin{bmatrix} \cos \frac{\psi}{2} & 0 & 0 & \sin \frac{\psi}{2} \end{bmatrix}^T, \quad (19)$$

where ψ is the actual Euler yaw angle of Z-Y-X convention. The altitude controller can be simply derived from (11)(12) with the assumption that $\mathbf{b}_3 \approx \mathbf{b}_{3d}$ as follows:

$$\mathbf{f} = -k_p(\mathbf{r}_3 - \mathbf{r}_{d3}) - k_d\dot{\mathbf{r}}_3 - k_i \int (\mathbf{r}_3 - \mathbf{r}_{d3})dt + m\mathbf{g}, \quad (20)$$

where \mathbf{r}_3 is the third component of \mathbf{r} and \mathbf{r}_{d3} is the desired altitude.

The results of the altitude and attitude control experiment are illustrated in Fig. 4 including the desired and measured altitudes and the Euler angles. It is clear that the attitude control algorithm (10) enables the direction of the thrust force approximately perpendicular to the \mathbf{n}_1 - \mathbf{n}_2 plane. Also angular oscillation occurs in the range of $[-10^\circ, 10^\circ]$, which

is acceptable in the sense that the magnitude of the lift force is not greatly reduced by the attitude oscillation as demonstrated in the experiment. Additionally, the robot reaches the desired altitude rapidly as shown in Fig. 4-A despite the static altitude error. The time lapse of the corresponding experiment is demonstrated in Fig. 5-A, which indicates that the flapping of the four wings generates enough lift force for the robot to take off and maintain its attitude upright for a long period of time. The drifting phenomenon is expected due to the lack of control on the \mathbf{n}_1 - \mathbf{n}_2 plane. Overall, the altitude and attitude control experiment verifies the effectiveness of the design and fabrication of this four-winged insect-scale flying robot, and demonstrates that the robot is able to perform controlled flight freely without being hanged for a long period of time.

C. Position Control Experiment

In this experiment, the insect-scale flying robot is commanded to hover at a desired position in the space, in which the attitude controller (10) and the position controller (11)(12) are implemented. Same as the altitude and attitude control experiment, the desired yaw angle is set to be the true yaw angle, i.e. $\psi_d = \psi$, which does not affect the position control since the direction of the thrust force is irrelevant to the yaw angle. The result of the position control experiment is demonstrated in Fig. 6, and the corresponding time lapse of the experiment is illustrated in Fig. 5-B.

Figure. 6-A shows the controlled position along with the reference signals, from which the robot is observed to approximately track the reference signals in the first second, then the position error on \mathbf{n}_1 axis gradually increases. In Fig. 6-B, the roll and pitch angle tracking in the first second are, to some extent, accurate, then the pitch tracking error gradually becomes large, which is consistent with the increase of the position error on \mathbf{n}_1 axis in Fig. 6-A. It is hypothesized that the oscillation about pitch axis is caused by the saturation of the actuators. This problem can be solved by improving the robotic design using the method in [23] to generate more available thrust force for position regulating or trajectory following flight control.

The complete set of experiments is presented in the supplementary Movie S1.mp4, which is also available at <https://www.uscaml.com/resources/IROS2019/S1.mp4>.

VI. CONCLUSIONS

We presented Bee⁺, a new 95-mg four-winged insect-sized flying robot with an extremely compact configuration, and the associated design and fabrication process. The proposed approach has numerous advantages in terms of weight, dimensions, aerodynamics, control and fabrication. The key innovation, and core component, that enabled the development of Bee⁺ is a new actuation technique based on the use of pairs of twinned unimorph actuators. As a step of the design process, by employing instantaneous and time-averaged quasi-steady analyses, we estimated the main aerodynamic characteristics of the robotic design, including ranges for thrust forces, damping and steering torques. Also, three different strategies for yaw-torque generation were discussed and we determined that the inclined stroke-plane method is the most appropriated for the control of the four-winged Bee⁺. Finally, we presented a method for controller synthesis based on techniques developed for quadrotors and real-time control experiments. In specific, we demonstrated the suitability and effectiveness of the methods for actuation and control through a real-time altitude-and-attitude regulation experiment and a real-time position

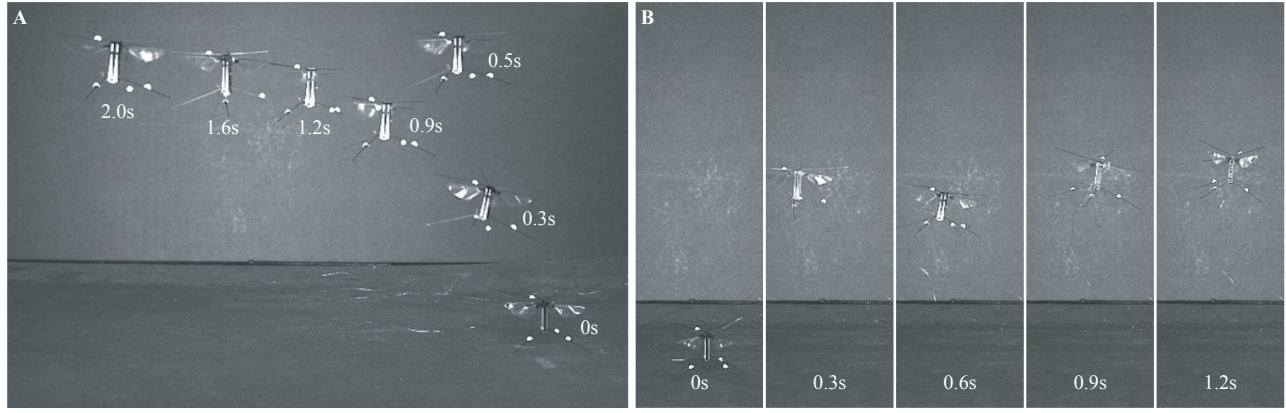


Fig. 5: **A.** The time-lapse plot of the altitude and attitude control experiment. The corresponding altitude and Euler angles are demonstrated in Fig. 4. During the experiment, the direction of the thrust force is controlled to remain approximately perpendicular to the n_1 - n_2 plane. The cable tethered to the robot provides the power and control signals. The robot drifts on the n_1 - n_2 plane due to the lack of control of the position. After 2 s, the robots flies out of focus area of the camera. **B.** Image sequences of the position control experiment. The corresponding position and Euler angles of this experiment are plotted in Fig. 6. The images are captured with the identical view position.

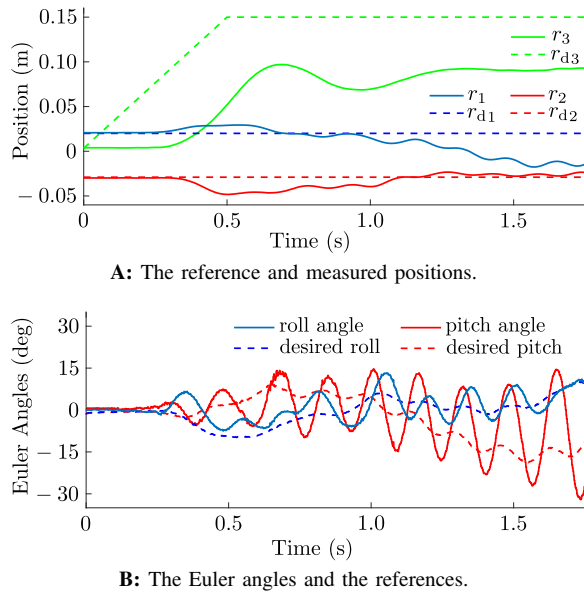


Fig. 6: The position control experiment result. **A.** The dash lines represent the desired position, and the solid lines represent the measured position. **B.** The dash lines represent the desired Euler angles derived from (13)(14)(15). The solid lines represent the measured Euler angles.

control experiment. In the future, the process of thrust-force generation will be improved by employing the method in [23] and we expect to achieve lift-to-weight ratios as high as 3. These developments will enable Bee⁺ to increase its available thrust force in order to perform aerobatic maneuvers and other complex flight tasks. In addition, the *clap-and-fling* phenomenon observed in the supporting movie S1.mp4 will be investigated as this aerodynamic mechanism can lead to a lift increase as large as 20%.

REFERENCES

- [1] M. A. Graule, P. Chirarattananon, S. B. Fuller, N. T. Jafferis, K. Y. Ma, M. Spenko, R. Kornbluh, and R. J. Wood, "Perching and takeoff of a robotic insect on overhangs using switchable electrostatic adhesion," *Science*, vol. 352, no. 6288, pp. 978–982, 2016.
- [2] S. B. Fuller, "Four wings: An insect-sized aerial robot with steering ability and payload capacity for autonomy," *IEEE Robot. Autom. Lett.*, vol. 4, no. 2, pp. 570–577, 2019.
- [3] M. H. Dickinson and M. S. Tu, "The function of dipteran flight muscle," *Comp. Biochem. Phys. A*, vol. 116, no. 3, pp. 223–238, 1997.
- [4] R. J. Wood, "Design, fabrication, and analysis of a 3DOF, 3cm flapping-wing MAV," in *Proc. 2007 IEEE Int. Conf. Intell. Robot. Syst.*, 2007, pp. 1576–1581.
- [5] N. O. Pérez-Arancibia, K. Y. Ma, K. C. Galloway, J. D. Greenberg, and R. J. Wood, "First controlled vertical flight of a biologically inspired microrobot," *Bioinspir. Biomim.*, vol. 6, no. 3, p. 036009, 2011.
- [6] K. Y. Ma, S. M. Felton, and R. J. Wood, "Design, fabrication, and modeling of the split actuator microrobotic bee," in *Proc. 2012 IEEE Int. Conf. Intell. Robot. Syst.*, 2012, pp. 1133–1140.
- [7] M. Oppenheimer, D. Doman, and D. Sigthorsson, "Dynamics and control of a biomimetic vehicle using biased wingbeat forcing functions: Part i-aerodynamic model," in *48th AIAA Aero. Sci. Meet.*, 2010, p. 1023.
- [8] K. Y. Ma, P. Chirarattananon, S. B. Fuller, and R. J. Wood, "Controlled flight of a biologically inspired, insect-scale robot," *Science*, 2013.
- [9] A. Roshanbin and A. Preumont, "Yaw control torque generation for a hovering robotic hummingbird," *Int. J. Adv. Robot. Syst.*, 2019.
- [10] M. Karásek, F. T. Muijres, C. D. Wagner, B. D. Remes, and G. C. de Croon, "A tailless aerial robotic flapper reveals that flies use torque coupling in rapid banked turns," *Science*, 2018.
- [11] B. M. Finio and R. J. Wood, "Open-loop roll, pitch and yaw torques for a robotic bee," in *Proc. 2012 IEEE Int. Conf. Intell. Robot. Syst.*, 2012, pp. 113–119.
- [12] N. T. Jafferis, M. J. Smith, and R. J. Wood, "Design and manufacturing rules for maximizing the performance of polycrystalline piezoelectric bending actuators," *Smart Mater. Struct.*, vol. 24, no. 6, p. 065023, 2015.
- [13] L. Chang and N. O. Pérez-Arancibia, "Time-averaged dynamic modeling of a flapping-wing micro air vehicle with passive rotation mechanisms," in *AIAA Atmos. Flight Mech. Conf.*, 2018, p. 2830.
- [14] —, "The dynamics of passive wing-pitching in hovering flight of flapping micro air vehicles using three-dimensional aerodynamic simulations," in *AIAA Atmos. Flight Mech. Conf.*, 2016, p. 0013.
- [15] B. Cheng and X. Deng, "Translational and rotational damping of flapping flight and its dynamics and stability at hovering," *IEEE Trans. Robot.*, vol. 27, pp. 849–864, 2011.
- [16] D. B. Doman, M. W. Oppenheimer, and D. O. Sigthorsson, "Wingbeat shape modulation for flapping-wing micro-air-vehicle control during hover," *J. Guid. Cont. Dynam.*, vol. 33, no. 3, pp. 724–739, 2010.
- [17] M. Sitti, D. Campolo, J. Yan, and R. S. Fearing, "Development of PZT and PZT-PT based unimorph actuators for micromechanical flapping mechanisms," in *Proc. 2001 IEEE Int. Conf. Robot. Autom.*, vol. 4, 2001, pp. 3839–3846.
- [18] R. J. Wood, S. Avadhanula, R. Sahai, E. Steltz, and R. S. Fearing, "Microrobot design using fiber reinforced composites," *J. Mech. Design*, vol. 130, no. 5, p. 052304, 2008.
- [19] Y. Chen and N. O. Pérez-Arancibia, "Nonlinear adaptive control of quadrotor multi-flipping maneuvers in the presence of time-varying torque latency," in *Proc. 2018 IEEE Int. Conf. Intell. Robot. Syst.*, October 2018, pp. 1–9.
- [20] A. Roberts and A. Tayebi, "Adaptive position tracking of VTOL UAVs," *IEEE Trans. Robot.*, vol. 27, no. 1, pp. 129–142, 2011.
- [21] Y. Chen and N. O. Pérez-Arancibia, "Generation and real-time implementation of high-speed controlled maneuvers using an autonomous 19-gram quadrotor," in *Proc. 2016 IEEE Int. Conf. Robot. Autom.*, May 2016, pp. 3204–3211.
- [22] P. Chirarattananon, K. Y. Ma, and R. J. Wood, "Adaptive control of a millimeter-scale flapping-wing robot," *Bioinspir. Biomim.*, vol. 9, no. 2, p. 025004, 2014.
- [23] N. T. Jafferis, M. A. Graule, and R. J. Wood, "Non-linear resonance modeling and system design improvements for underactuated flapping-wing vehicles," in *Proc. 2016 IEEE Int. Conf. Robot. Autom.*, 2016, pp. 3234–3241.